

# LOCAL STRUCTURAL ORIENTATION OF TOWEL AND TISSUE GRADES IN TWO AND THREE DIMENSIONS

*D. S. Keller<sup>1</sup>, C. Feng<sup>1</sup>, J.-F. Bloch<sup>2</sup> and  
S. Roland du Roscoat<sup>3</sup>*

<sup>1</sup> Miami University, Department of Chemical, Paper, and Biomedical  
Engineering, Oxford, OH, USA

<sup>2</sup> Grenoble Institute of Technology, 38402 Saint Martin d'Hères, Cedex,  
France

<sup>3</sup> Université Joseph Fourier, Domaine Universitaire, 38041 Grenoble  
Cedex, France

## ABSTRACT

This paper describes the study of new methods for characterizing the orientation of fiber segments in low density paper towel from two- and three-dimensional X-radiographic data sets. The end use properties of the absorbent hygiene grades such as paper towels and tissues stem from an open porous structure where stochastically distributed fibers are contorted by post forming processes to increase bulk, stretch, flexibility and softness, while maintaining adequate strength. The orientation of free fiber segments that form the network are kinked and curved in three dimensions by processes including creping, through air drying and embossing. Providing a linkage between process conditions and the end use properties through the characterization of the network structure is the overarching goal of this investigation. A method is presented for mapping the 2D, in-plane orientation of fiber segments using soft (6kV) X-radiographs and an algorithm for calculating the image moments for circular sub-regions that surround each point. The eigenvectors form the major and minor

axes of the inertial ellipse from which the principal orientation may be extracted. Colorized maps representing the local orientation are used to examine the effects of embossing and creping, as well as comparing different forming processes. A method for characterizing fiber segment orientation in three dimensions uses a similar approach applied to binarized X-ray micro-computed tomographic data sets. The inertial ellipsoid is determined by performing principal component analysis on the covariance matrix of the voxels contained within a spherical region surrounding each solid voxel within the structure. The eigenvectors are used to extract the shape and principal orientation of the ellipsoids which are plotted as colorized representations in 3D space. The 2D and 3D plots demonstrate the sensitivity of the method to orientation of fiber segment mass, while mean fiber orientation plots reveal differences between samples.

## **INTRODUCTION**

It is well known that for fibrous webs, including paper, that the orientation of the fibers within the structure has a direct influence on the bulk material properties, especially mechanical behavior and dimensional stability. For most communication papers and packaging papers and paperboards, having densities that range from  $550 \text{ kg/m}^3$  to  $1000 \text{ kg/m}^3$ , the fiber length is from 10 to 100 times the web thickness causing fibers to be stratified within the structure. Depending on the hydrodynamic flows and energy imparted by the forming elements, the fibers tend to be preferentially oriented, to a greater or lesser extent, towards the machine direction. For many grades the machine direction orientation is intentionally increased using the velocity difference between the stock jet and the wire(s), to enhance mechanical strength in the machine direction in order to improve runnability during coating, web printing or in roll converting operations. Orientation may also be imparted for sheeted grades, such as uncoated wood free, so that curl can be controlled during sheet fed printing or copying. For these situations, it is usually sufficient to determine the mean fiber orientation, or the anisotropy of the web using angle dependent tensile strength measurement or by measuring the angular dependent tensile stiffness using ultrasonic transmission [1, 2]. The examination of local fiber orientation MD streaks, and more specifically the optical scanning of formation of different Z-direction strata using sheet splitting [3], has helped to identify the origin of MD curl defects in copy paper and paperboard. The origin of such streaks was found to originate in the cross flows of the stock as it exits the slice of the headbox and subsequently led to the development of the dilution headbox [4, 5].

Low density paper grades including tissues, towels and hygienic wipes, with densities less than  $300 \text{ kg/m}^3$ , often have end use requirements, such as flexibility, softness, tensile strength and energy, stretch, and liquid absorptivity, that present design challenges for mutual optimization. For example, a high degree of chemical or mechanical debonding may be sought to impart bulk, internal surface area and flexibility. However, this counteracts the extent of interfiber bonding needed for mechanical strength in tension, for abrasive rub resistance and to prevent linting. Thus, the structure of tissue and towel papers is in general quite complex. It results from the stochastic deposition of fibers in forming, with subsequent processes that reposition fibers to increase bulk and localized bonding in order to gain strength and absorptivity. Unlike communication papers where value is placed on spatial uniformity of structural properties such as mass, density, thickness and mean fiber orientation, the tissue and towel grades benefit from induced structures such as creping, embossing and drying features that create non-uniformities in select ranges of scale, thereby enhancing the end use properties. In as such, the bulk properties of softness, strength and absorptivity measured in the  $10^{-1}$  meter scale range are determined by distributed structural characteristics between  $10^{-2}$  to  $10^{-6}$  meters. It is also important to consider that the induced structures, such as creping lines, through air dried (TAD) features and embossed patterns do not act in isolation, but are superimposed on the structure formed in all of the preceding process steps, including the fiber length and the uniformity of the initial formation. Thus the rearrangement of fibers in all three dimensions (MD, CD and ZD) depends on the extent of interfiber bonding and fiber flexibility as well as the forces imparting the deformation from processing. Fibers may be locally reorganized into regular patterns from the forming fabric, circular TAD patterns, oriented in the cross machine direction, or kinked in the Z-direction as a result of induced features. Since the extent of interfiber bonding for low density grades are much less than in printing and packaging papers, free fiber length is greater and the extent of confinement of fibers to planar strata is significantly lower. And while mean fiber orientation is generally considered sufficient to characterize the strength properties and curl tendencies of printing and packaging papers, the performance of tissue and towel papers depends more heavily on the orientation of individual fibers in three dimensions, in and around induced features that are typically less than 5 mm.

The purpose of this investigation was to explore new methods for characterizing the local fiber orientation in low density fibrous structures, specifically paper towel products. These structures have less bonding and greater free fiber length as compared to communication and packaging grades, which makes them more conducive to segmentation and isolation of individual fibers when observed using 2D and 3D radiographic imaging. The novel approaches for measuring the local orientation described herein are based on measurement of the second order mass

moment for 2D images and principal component analysis of the covariance matrix of 3D tomographic representations. The methods were developed from concepts found in studies measuring and simulating fiber orientation in reinforced composite materials [6] and in biological structures [7]. While the most common approach applied to higher density paper grades is to apply spectral or statistical algorithms to determine an aggregate regional orientation distribution, in this study orientation is mapped locally for each discrete element of the imaging data set.

## **Structural Imaging Methods**

The two methods for acquiring data sets that have sufficient resolution to distinguish individual fiber features are both based on X-ray absorption. In this study, soft X-radiography was used to acquire 2D radiographic images. 3D data sets were obtained from X-ray micro-computed tomographic (XR- $\mu$ CT) imaging using both a synchrotron source beamline laboratory, and a laboratory scale high resolution X-Ray imaging system.

### *Soft X-radiography for 2D Imaging*

Since tissue and towel samples usually contain no minerals, or in the case of recycled products exceedingly low concentrations, the attenuation of X-rays can be attributed solely to carbohydrates and therefore may be used to closely approximate the mass in a given spatial region by the Beer-Lambert law by the equation:

$$I = I_0 e^{-\kappa' w} \quad (1)$$

The transmitted radiation intensity,  $I$ , is a function of the incident radiation,  $I_0$ , the mass absorption coefficient,  $\kappa'$  ( $\text{m}^2\text{g}^{-1}$ ), and the grammage,  $w$  ( $\text{g m}^{-2}$ ), for a material of uniform density.

Traditional radiographic methods for capturing formation maps using contact  $\beta$ -radiography [8–10] are unsuitable for the thick web samples tested in this study, since the radioactive plate acts as a diffuse source  $\beta$ -ray emitter yielding images with poor depth of field. Pawlak and Keller [11] demonstrated that resolution of fiber features is lost as distance to the detector, i.e. film or imaging screen, is increased. A soft X-ray tube can be used to avoid this problem by emitting a near point source energetic beam where the relative distance from the source to the samples is much greater than from the sample to the detector, i.e. film. The sample is illuminated by a narrow cone of radiation that results in a relatively sharp fiber edge definition and excellent spatial fidelity through the entire thickness ( $< 2\text{mm}$ ) of the paper towel samples. Soft X-radiation (1keV to 10keV) is used for low

atomic weight and thin materials such as paper, since it provides ample gray level contrast and thus, better precision of grammage values. By using X-ray film and high resolution scanning, the transverse dimensions of individual pulp fibers can be clearly detected at the upper and lower surfaces of towel samples, as demonstrated in the radiograph shown in Figure 1.

Soft X-Radiography has been applied to paper for more than fifty years, as first reported by Pelgrams [12], with the most recent relevant research using the method by Tomimasu et al. [13], Farrington [14] and Yuhara et al. [15–17]. The latter two investigators used soft X-radiography to study the mean fiber orientation using two-dimensional power spectral analysis. Their application of the method was limited in detected spatial resolution, so that rather than fiber geometry, the micro-scale variation in grammage was used in the analysis. Furthermore, they did not apply sufficient correction for spatial non-uniformity of the incident radiation to enable direct conversion to grammage. The acquisition of grammage maps with sufficiently high spatial and grammage resolution depends on the ability to correct the spatially dependent artifacts inherent to X-radiography. The implementation of an appropriate correction strategy was the subject of work conducted by Feng [18], and was applied to the images used in this study.

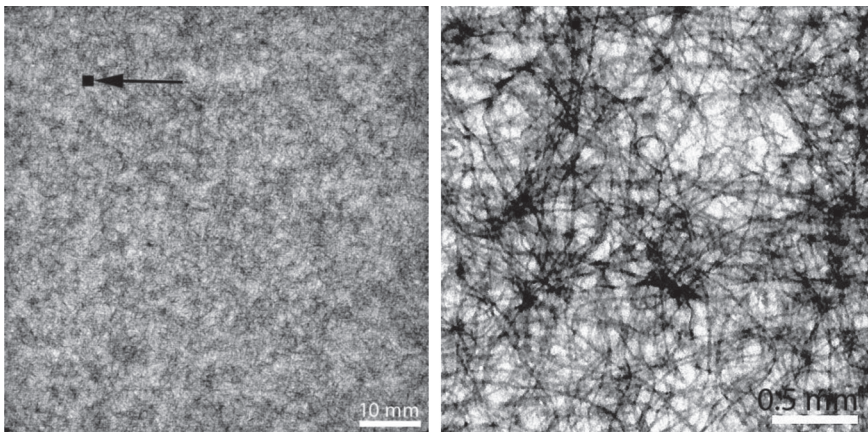


**Figure 1.** An example of the resolution that is observed using the high resolution X-radiographic method. High mass absorption is shown as black. The image on the left is  $75 \times 75 \text{ mm}^2$  region of a radiograph scanned at  $5.3 \mu\text{m}/\text{pixel}$ . The image on the right shows a zoomed region (indicated by the arrow on the left). Note that the fiber width is clearly visible from the darkened, high mass edges of the collapsed tubular structure of the fibers.

### *X-Ray $\mu$ -Computed Tomography (XR- $\mu$ CT) for 3D Imaging*

X-Ray micro-computed tomography was found to be well suited for the analysis of low density web structures as investigated by Keller et al.[19]. Three dimensional representations of the paper towel samples were obtained from X-ray micro-computed tomographic (XR- $\mu$ CT) imaging using both synchrotron based facilities and commercially available X-Ray imaging instruments. The methods for obtaining 3D representations using the radon transform of multiple projections from highly collimated X-ray illumination is described in detail elsewhere [20]. The data sets required preprocessing to obtain data sets with clear segmentation between void space and sample fibers.

### **Orientation of Local Fiber Segment**

The literature has numerous examples for determining the structural characteristics, i.e. position, orientation, curvature and cross sectional geometry, of fibers within web structures. A common approach has been to track individual fibers that have been successfully segmented from the bulk structure [6, 21–24]. Examples of isolated fiber segments are illustrated in Figure 2 [24]. While in principle, this method could reveal a comprehensive representation of all spatial aspects of the fiber configuration, it is usually only achieved by making assumptions about the fiber cross sectional geometry, estimating fiber-fiber contacting area, and special handling of discontinuities such as kinks, partial fractures and the bonding of fibers that are closely aligned. Axelsson [25] determined the orientation distribution of synthesized gray scale test volumes of tubular fibers in order to simulate wood fibers. A series of six quadrature filters, each sensitive to a specific orientation, was used to estimate the local orientation and construct a structure tensor at each voxel position. The eigenvectors and eigenvalues of each tensor were used



**Figure 2.** Examples of isolated fibers segmented from a XR- $\mu$ CT representation of a fibrous structure [24].

to calculate local fiber orientation, which was then averaged over regions of interest to determine the orientation distributions of sub-volumes. Wiltsche et al. [22] suggested the use of centroids of the cross sections of individual segmented fibers to track the position in space, from which the distribution of 3D fiber orientation was tracked. Using a different approach to arrive at similar outcomes, Tan et al [26] characterized sintered metallic fibers by first segmenting, and then generating the external surfaces of the solid fibers. These surface shells were then “skeletonized” to determine the position of the medial axes. These two tracking methods may be found valuable for characterizing low density tissue and towel web structures from 3D tomographic data sets, since the fiber count is low and fibers are more readily isolated from the structure.

The investigation conducted by Altendorf [6, 7, 27] used the determination of the inertial ellipsoid from the directed distance transform at each solid voxel within 3D representations of glass fiber and carbon fiber reinforced composites, and collagen fibers in hydrogel matrix. The distance transform determines the distance along a chosen direction between the starting voxel and the boundary between solid matter and void space [27]. For a complete adjacency system, distance is determined in 26 directions for 13 chords, where chord length is determined by summing the line segments in opposing directions. The 13 chords are then used to calculate the first and second moments, from which an ellipsoid with the eigenvector having the highest eigenvalue constitutes the major axis of orientation in space. The aspect ratio of the ellipsoid indicates the intensity of orientation along the major axis. Since the fibers examined by Altendorf et al. [7] had a circular cross section, they also mapped the local fiber radius and determined the radius distribution for a given region. The directed distance transform for binarized data sets [27] and the quasi distance transform developed for gray level data sets [7] were both considered unsuitable for the samples examined in this study for several reasons. First, the cross sectional geometry of collapsed woody fibers is complicated by defects, such as anatomical pits, kinks and folds. Collapsed lumens that vary in thickness along the length of the fiber also present problems for calculating chords that are transverse to the fiber. Secondly, while this method is robust, it is also computationally inefficient for determining the moments at each solid voxel. In this study an alternate method for determining the inertial ellipsoid was used.

### **Fiber segment orientation from moments of inertia**

The method developed for mapping the local orientation of fibers in this study is based on the calculation of the local geometric moments for defined regions that surround each 2D or 3D image element. For the two-dimensional case, the second order image moments are calculated and used to determine the parameters of the

inertial ellipse with tilt angle and eccentricity that indicates the orientation of mass within the sampled circular region, cf. Figure 3. The region is, of course, a representation of the integrated mass of the fibrous structure through the z-direction. The equations for this analysis are provided in Appendix 1. Inertial ellipses are determined for each pixel within the image, so that maps for the ellipse parameters can be compiled for the entire sample. The local variation of these parameters due to the forming or post forming process may then be quantified by examining sub-regions of the sample area. The orientation distribution for the entire sample or for selected regions is determined by generating a histogram of the orientation angles for all pixels within the sample area or a sub-region thereof.

For tomographic data sets represented in three-dimensional space, the covariance matrix of distance to the center voxel for all solid voxels contained within the spherical region of interest is determined, and principal component analysis (PCA) is then performed to determine the center of mass and the lengths of the three orthogonal axes of an inertial ellipsoid. The axis rotation matrix from PCA is readily converted to the Euler angles that represent the orientation of this ellipsoid in three-dimensional space. The orientation angles of the principal axis,  $a$ ,

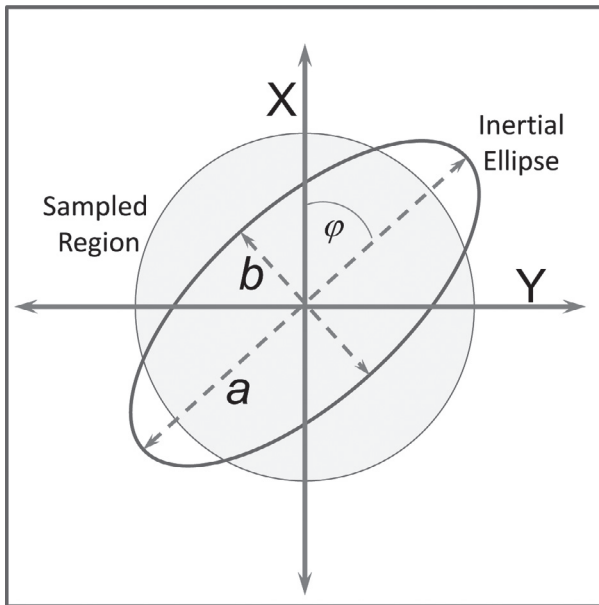


**Figure 3.** Two dimensional inertial ellipse as determined from the second moments of the points contained within the circular region. Ellipse parameters include the length of the major axis,  $a$ , and minor axis,  $b$ , and the orientation angle,  $\varphi$ .

provide the direction of mass alignment, while the ellipsoid dimensions may be used to determine the intensity of orientation. Figure 4a illustrates how this would be calculated from a  $5 \times 5 \times 5$  voxel<sup>3</sup> matrix with the center shown in yellow. The voxels within this region that have no mass, nor connectivity with the center voxel are excluded. Voxels that fall within a defined spherical region, shown in darker blue, are then used in to calculate the inertial ellipsoid that is lightly outlined. The background of Figure 4a shows an actual representation of the colorized 3D structure of a fibrous structure where voxel color indicates the in-plane orientation angle,  $\varphi$ . Figure 4b illustrates the angles used in this study formed by the principal

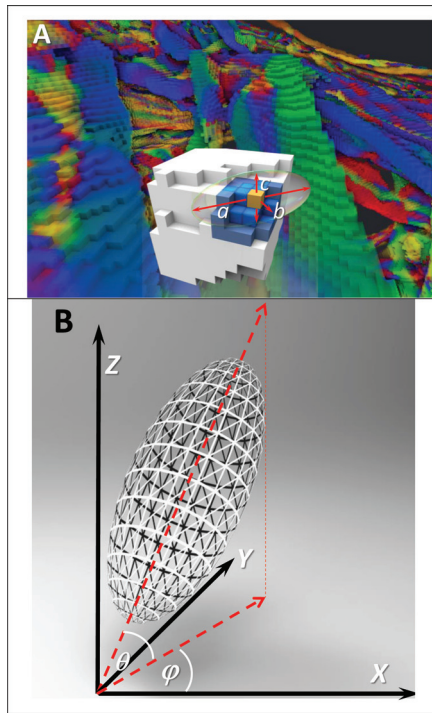


**Figure 4.** Three dimensional representation of the method used to determine the inertial ellipsoid for each voxel within the test region (represented here by the entire structure). The inset sketch in Fig 4a shows inertial ellipsoid formed from the PCA method, that has three orthogonal axes of decreasing length,  $a$ ,  $b$ , and  $c$ . The background shows an actual representation of a 3D structure as calculated in this study, where each voxel is colored according to the in-plane orientation (azimuth). Fig 4b illustrates the Euler angle for azimuth,  $\varphi$ , for orientation within the X-Y plane that is the principal plane of the sample, and for elevation,  $\theta$ , that indicates out-of-plane inclination in the Z-direction.

eigenvector,  $a$ , with the principal plane of the material. In this study, the principal plane is considered the hypothetical plane formed by the mean MD and CD axes for the sampled region. The in-plane orientation,  $\varphi$ , and the elevation from that plane,  $\theta$ , are used to characterize the mass at each voxel. As we hypothesized in this study, the aspect ratio of an ellipsoid formed from voxels located along an edge is more elongated along the principal axis than for voxels in planar regions or for those found at the intersections of fibers. This can be used to segment mass in different regions. As with the 2D case, orientation distributions, for fiber orientation along each of the three orthogonal axes, may be determined for selected regions by generating a histogram of the orientation angles for all pixels within the sample area.

## **MATERIALS AND METHODS**

### **Materials**

The samples examined in this study were commercially available paper towels, both one and two-ply. The samples were selected as representative of various manufacturing methods including conventional wet pressed (CWP) and various through air dried (TAD) products where the web structure is formed using patterned belts. Samples were tested after conditioning according to TAPPI Test Method T-402 standard conditioning (50%RH, 23°C). Two-ply samples were carefully separated and identified as the top or bottom ply, where the top is identified as the side the faces outward for converted rolls. Samples are identified in Table 1. where the values for gravimetric grammage as measured by TAPPI standard methods T410 [28] and flat platen thickness, using T411 [29] are provided. The mean X-radiographic grammage as determined by the method discussed below is also given in Table 1 for comparison with gravimetric grammage. The thickness determined by non-contact optical mapping using the twin laser profilometer [30] is also shown in the table. Thickness determined by this method is considered more representative of the non-compressed fibrous web thickness and not the peak to base thickness of embossed or TAD induced features.

### **X-Radiography for 2-Dimensional Imaging**

#### *Soft X-Radiography*

Samples were tested using a Minishot X-Ray cabinet (Associated X-Ray Corporation East Haven, CT) to expose Structurix D2 (Agfa) X-ray film. Samples were placed in a restraining frame to expose an  $80 \times 80 \text{ mm}^2$  area. Adjacent to the

**Table 1.** Paper Towel Samples tested in this study

		<i>XR-<math>\mu</math>CT</i>	<i>Grammage</i> <i>G (g/m<sup>2</sup>) R</i>		<i>TAPPI Std.</i> <i>Caliper</i> <i>(<math>\mu</math>m)</i>	<i>Non-contact</i> <i>TLP Thickness</i> <i>(<math>\mu</math>m)</i>
T1	TAD-1 2-ply, top	Beck	28.8	31.0	155	108
T2	TAD-2 1-ply	Beck, Xrad, ESRF	39.2	40.7	196	38
T3	TAD-3 2-ply, top	XRad, ESRF	21.5	22.9	140	71
T4	TAD 4 2-ply, top	ESRF	30.0	31.1	235	73
T5	TAD 5 1-ply	ESRF	39.1	40.7	300	127
A1	ATM 1 2-ply, top	Beck	24.7	25.1	105	–
C1	CWP 1 2-ply, bot.	ESRF	22.8	22.5	125	23
C2	CWP 1 2-ply, bot	ESRF	21.9	22.77	100	29

Grammage: G–gravimetric; R–2D radiographic

sample, the frame also held five Mylar films that spanned the range of grammage tested in this study. This was used as an internal standard from which calibration curves were generated for each exposure. Samples were exposed for 16 min at 6 kV and 4.5 mA. Exposed films were developed manually using chemicals from H.R. Simon and Company. Films were scanned in transparency mode at 4800 dpi (5.3  $\mu$ m pixel size) and 16 bit gray level depth using an Epson V700 high resolution scanner. A sample frame was used to separate the film from the scanner glass in order to prevent internal reflection that causes Newton rings to form in the detected image.

### Image Preprocessing

The raw radiographic images have a spatial non-uniformity of exposure due to the isoplanatic distribution of intensity, referred to as vignetting, and an artifact of the electron beam/target interaction that causes a directional variation of intensity, called the “heel effect”. Preprocessing of the images addressed both artifacts before images were analyzed. The heel effect was corrected using the relationships provided by Behiels et al. [31] and Fritz and Livingston [32]. The heel effect was found to have only a small effect on spatial non-uniformity for the method used in this study due to the low energy of the X-rays, i.e. 6kV. The vignetting distortion was corrected by using the so called “Cos<sup>4</sup> Law of Illumination” [33] which uses the fixed focal-film distance (FFD), i.e. the distance between the X-ray source and the film, to determine the beam intensity as a function of

distance from the center of illumination. The mitigation of the spatial intensity artifacts was verified for each sample by examining the mean intensity profile for 5 mm bands (vertical and horizontal) that pass through the center of the image. The grammage maps for each radiographic image were calculated by using the gray scale value at each location and the calibration curves created from the associated Mylar step wedge. 16 bit Gray level tiff image files were used to calculate 2D orientation after scaling the intensity histogram to maximize contrast.

### *Image Analysis: 2D Orientation*

The 2D orientation mapping was performed using custom function written in Matlab 12b (The Mathworks Inc.) on an HP Z600 Workstation computer. Essentially, the routine involved iteratively stepping through each pixel within the sample image, selecting a sub-region of neighboring pixels for use in second moment calculations, determine the lengths of the major and minor axes, and the mean orientation angle of the ellipse formed between the major axis and the X-axis (MD) for the sample. Figure 5 illustrates the specific constraints used in this study for all samples. Image A shows a square radiograph with sides of 5.3 mm (1000 pixels). Images B and C show enlargements of the windowed sub-region having sides of 0.265 mm (5 pixel). This region is resampled with a bicubic interpolation to reduce the pixel size by a factor of 10 to 0.53  $\mu\text{m}$  (see image D). A mask is then applied to include only the central circular region surrounding the center pixel. The second moment of inertia and the parameters defining the characteristic orientation ellipse, cf. Figure 5 E, are then calculated using equations 5–10 in Appendix I, and modifications of the MATGEOM Geometric Computing Toolbox [34]. One modification was to recode the functions to run in parallel on multi-core processors. The results are presented as maps of the local orientation,  $\varphi$ , major axis length,  $a$ , minor axis length,  $b$ , and the aspect ratio of the ellipse ( $a/b$ ) at each pixel within the sample image. For this study, square samples with sides of 1000 pixels, 2000 pixels and 4000 pixels were analyzed for various samples. The mean orientation distributions for samples are presented by plotting the angular histogram on polar plots.

## **X-Ray Micro-Tomography for High Resolution 3-Dimensional Imaging**

### *Synchrotron XR- $\mu$ CT*

The European Synchrotron Radiation Facilities (ESRF) in Grenoble, France was used to obtain three dimensional tomographic data sets using the experimental

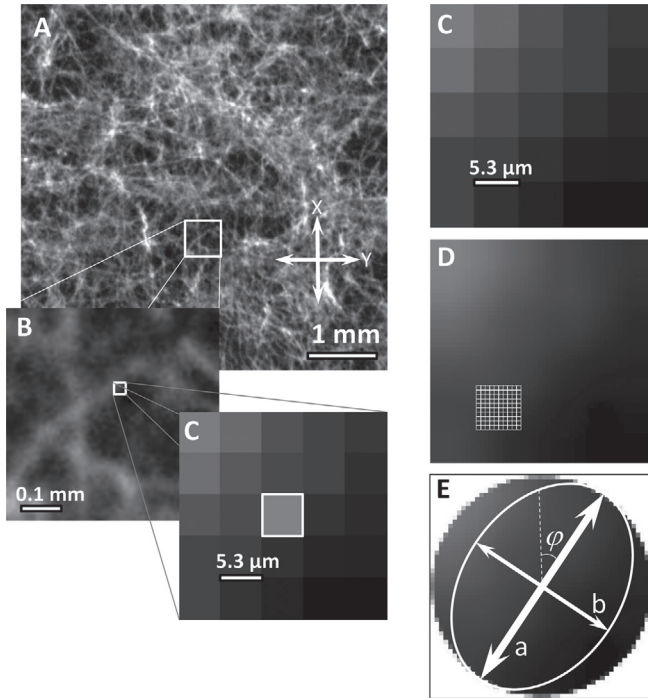


**Figure 5.** An illustration of the method used to map the 2D orientation using X-radiographic images. Image A shows a 5.3 mm square region with pixel size of 5.3  $\mu\text{m}$ . Image B provides an indication of the spatial resolution of the imaging methods and its ability to resolve fibers. Image C shows the  $5 \times 5$  pixel window within the image moment is determined. The windowed region is sub-sampled by a factor of 10 to ensure that the circular mask has the correct shape. The inertial ellipse is determined for that circular region where the orientation angle,  $\varphi$ , and lengths of the major and minor axes are recorded at the position of the center pixel shown in image C.

method described in detail by Roland du Roscoat et al. [20]. Table 1 shows the samples used in this study, and indicates the source and resolution of the XR- $\mu$ CT data sets. The samples were affixed to a stage, and rotated within the beam path around an axis perpendicular to the principal plane of the sample and tested to a voxel size of 0.7  $\mu\text{m}$ . The data sets generated by this method contain a cylindrical region, with in-plane dimensions of  $2048 \times 2048$  pixel<sup>2</sup> ( $1.4 \times 1.4$  mm<sup>2</sup>), and vertical slices, spaced at 0.7  $\mu\text{m}$  apart, sufficient to fully envelop the sample thickness.

### *Laboratory Instrument XR- $\mu$ CT*

Three dimensional data sets were obtained from two separate facilities, both using MicroXCT-200 (XRadia, Pleasanton, CA) 3D X-Ray Imaging System. One sample series was tested at the XRadia corporate laboratories. Data from these tests had a voxel resolution of  $0.58 \mu\text{m}$ . These samples were imaged by rotating the sample around an axis parallel to the principal plane of the sample; resulting in rectangular regions with dimensions of  $2048 \times 2048$  pixels ( $1.16 \times 1.16 \text{ mm}^2$ ). Ringing artifacts were not observed. A second sample set was tested at the Imaging Technology Group, Beckman Institute at the University of Illinois (U-C campus). The data sets generated from this series had a voxel size of  $2.5 \mu\text{m}$  and imaged regions of  $1024 \times 1024$  pixels ( $2.5 \times 2.5 \text{ mm}^2$ ) in stacks of slices spaced  $2.5 \mu\text{m}$  apart.

### *Image Preprocessing*

The data sets received from the XR- $\mu$ CT source were received as files containing stacks of 8-bit gray scale images. Simple segmentation of the data was performed by first despeckling with a  $3 \times 3$  median filter, and then manually selecting and adjusting gray level values to a global high pass threshold value as described by Holmstad [35]. Ring artifacts at the periphery of the data obtained from the ESRF synchrotron was removed by applying a circular mask to all slices within a given data set. Preprocessing was performed using ImageJ software (NIH) [36]. The tomographic data sets were first binarized by thresholding to segment between solid mass and void space in preparation for calculation of 3D orientation.

### *Image Analysis: 3D Orientation*

Image processing and analysis was conducted on a Dell Precision T3600 workstation using Matlab 12b and Avizo (Visualization Sciences Group) software systems. The analytical routine involved identifying all of the solid containing voxels, and iteratively determining the orientation ellipsoid parameters for each within the entire sample region.

The orientation ellipsoid was determined from the moment of inertia for a spherical region surrounding the center voxel, as illustrated in Figure 4A. The sub-region size used in this study was  $21 \times 21 \times 21$  voxels<sup>3</sup>. The regions without direct connectivity to the center voxel were removed using a 6 vector flood fill. A spherical mask was then applied so that only mass contained within a defined radius, in this case 10, was included in the subsequent calculations. The inertia ellipsoid was calculated by computing the covariance matrix of points within the

spherical region and performing a principal component analysis using singular value decomposition. The Euler angles and dimensions of the ellipsoid were then determined from the axes rotation matrix using routines modified from the MATGEOM Geometric Computing Toolbox [34]. The orientation ellipsoid parameters for each solid voxel were consolidated as three dimensional spatial maps and stored in separately.

### *Data Representation*

The spatial distribution maps of 2D orientation, for  $\varphi$  in the x-y plane, are presented as four color maps. Green indicates an orientation in the x-direction ( $0^\circ$ ) and red indicating the y-direction ( $-90^\circ$  and  $+90^\circ$ ). Unless otherwise noted, the x-direction is viewed vertically in all figures and represents the machine direction of the paper samples. Yellow represents an angle of  $+45^\circ$  and blue an angle of  $-45^\circ$ . Figure 6 illustrates how fiber orientation may be visualized using this convention. The upper half of the figure shows an X-radiographic image of a paper towel in the right frame. The left frame contains geometric shapes including simulated fibers. The image consists of  $1000 \times 1000$  pixels. The lower half shows the results of 2D orientation analysis performed on the upper half. The color scale on the right indicates the orientation determined at each pixel within the image. It is evident that the angular orientations of the edges of the geometric shapes were adequately determined by this method. This can be seen for the linear spans of the octagon and the simulated fibers. It can also be seen for the curved edges of the circle where color continually varies with edge orientation. The simulated fibers, however, also show an artifact where the planar region between to edges appears to give orientation values that are perpendicular to the adjacent edges. For example, the external edges of the fiber are green, indicating an orientation of  $0^\circ$  over the length of the fiber. However, the center region is red, indicating an orientation perpendicular to the edges,  $+90^\circ$  or  $-90^\circ$ . This artifact will persist in 2D radiographic images of low density paper samples, since the collapse of the fibers tends to accentuate the fiber edges resulting in parallel lines with higher mass, cf. the radiograph in Figure 6. The corresponding 2D orientation map clearly demonstrates sensitivity to the details contained in the radiograph, and a reasonable approximation of the fiber segment orientation.

For representation of the 3D orientation, only two of the Euler angles are presented in this study;  $\varphi$  for orientation within principal x-y plane of the sample, and  $\theta$  indicating elevation, or inclination from the principal plane. The last Euler angle,  $\psi$ , measures the angle of roll of the ellipsoid about the major axis. The color scale indicating angle is the same as that used in the 2D analysis discussed above. However, color is applied at each position of the tomographic spatial representations. Two such representation were generated for each sample,

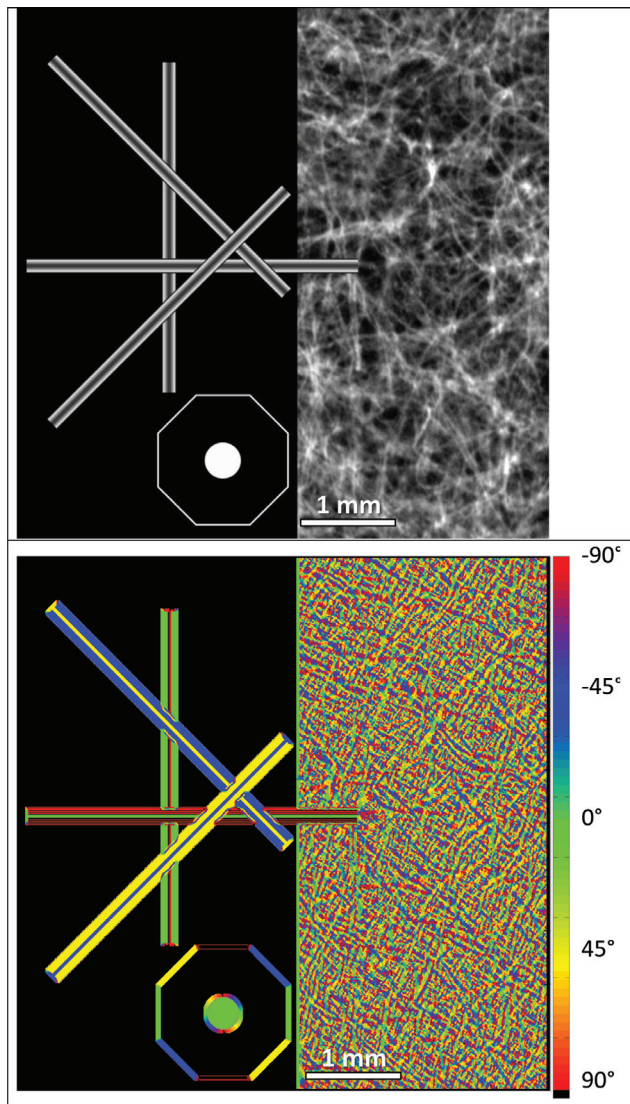


**Figure 6.** Example of the color scheme used to represent in-plane orientation,  $\varphi$ , for 2D orientation mapping. The upper half is a  $1000 \times 1000$  pixels template that includes a typical X-radiographic image of paper towel (right), and geometric shapes (left). The lower half shows the results from a 2D orientation analysis mapped using the standard convention.

mapping local in-plane orientation of fiber segments ( $\varphi$ ), and the elevation of the inertial ellipsoid at each position ( $\theta$ ).

## **RESULTS AND DISCUSSION**

### **2D Orientation Analysis**

#### *2D Orientation maps and histograms*

The results for 2D orientation analysis of a series of paper towel samples are presented in Figures 7, 9–10. For each sample a square region with sides of 10.6 mm (2000 pixels) was examined. Figure 7 shows the results for two through air dried (TAD) samples where the top frames show photographs of the samples taken at 30° light illumination in order to highlight the topography of the structural features. X-radiographs are shown in the center frames and the orientation maps in the bottom frames. Polar plots of the orientation distribution for the sampled regions are shown as insets in the orientation maps. The radiographs for the two samples clearly show the material displacement due to the TAD process that appears as enclosed shapes bounded by high grammage with diameters of about 2 mm. Higher grammage is observed due to the presence of the steeply inclined side walls of the feature, or by fiber displacement around the base of the feature during the TAD process. The details of the radiograph, including TAD features and individual fibers are replicated in the orientation maps shown for each of the two samples. At this scale, it is difficult to quantify the difference between the samples from the appearance of these maps. Close inspection reveals that the TAD-1 sample shows a greater population of fiber aligned approximately horizontal (cross machine direction), as compared to the TAD-2 specimen. These may be associated with fabric patterning that causes preferential alignment of the fibers prior to bond formation. It may also be caused by creping of the web that causes fibers to kink and corrugate in the cross machine direction where the observed material alignment is attributed to the inclined walls of the creped pattern. A clearer representation of the orientation of these samples is shown in the orientation distributions as the insets in Figure 7 (polar) and in Figure 8 (Cartesian) where the difference in material alignment observed in the orientation maps can be quantified. The TAD-2 sample has dominant orientation that is +15° of axis, while the TAD-1 shows considerably more material alignment that is perpendicular to the principal orientation at +15°.

The results for the next two TAD samples are shown in Figure 9. TAD-3 has material properties that are similar to TAD-1 and are different products made by the same manufacturer. The orientation maps are essentially indistinguishable,

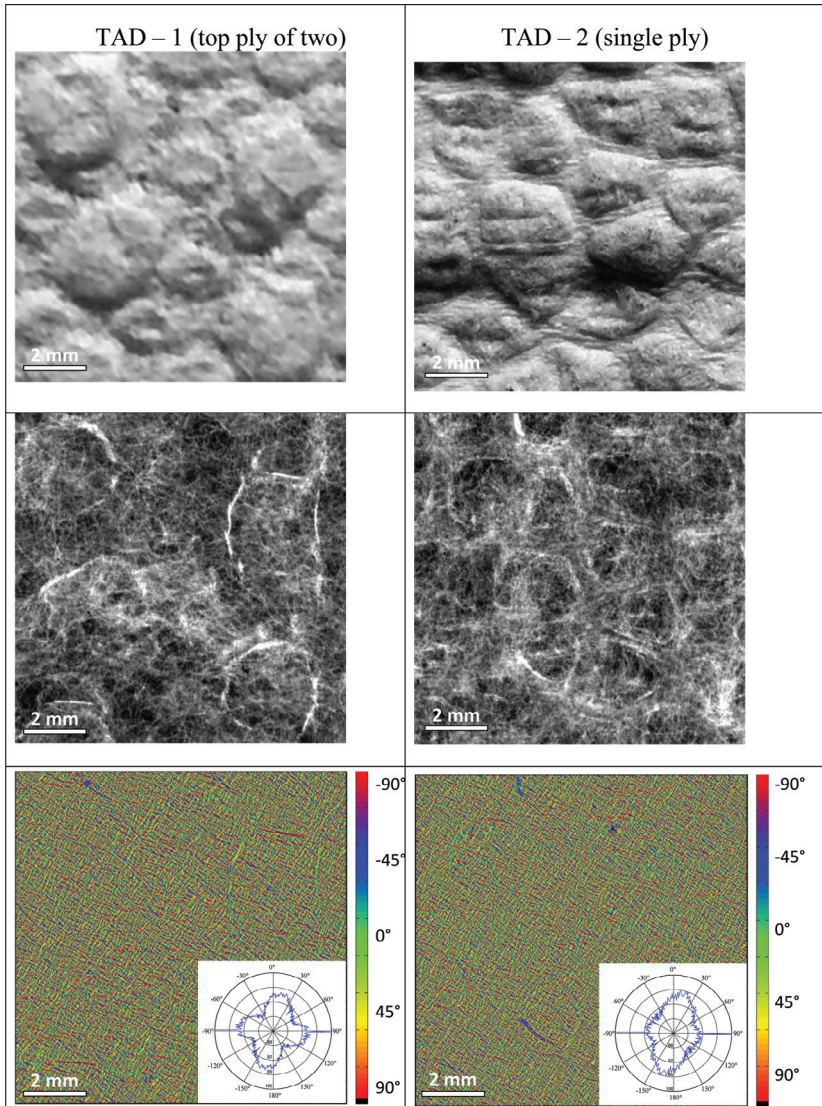


**Figure 7.** Two-dimensional orientation results for TAD - 1 (left) and TAD - 2 (right) paper towel samples. Top frame shows a photograph of the sample under 30° grazing angle light. The center image shows the soft X-radiographic images with side length of 10.6 mm. The lower frame shows the 2D orientation maps corresponding to the radiographic images above. An inset in the lower frame shows the polar orientation distributions for the data used to form the 2D orientation maps.

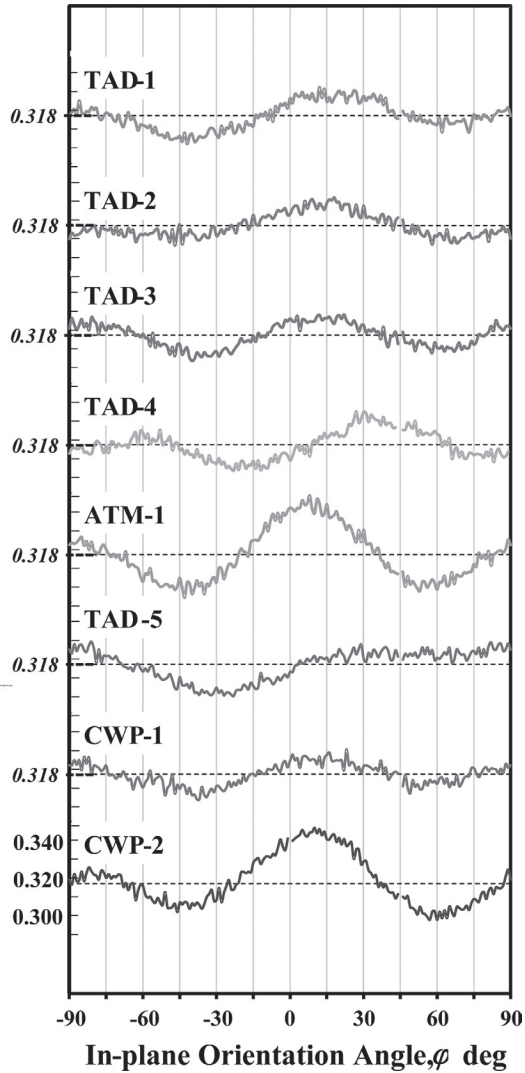


**Figure 8.** Orientation distributions for the 2D orientation maps generated from high resolution X-radiographs. The normalized probability density,  $\psi$ , is plotted as a function of in-plane orientation,  $\phi$ , where  $0^\circ$  is the machine direction of the sample.

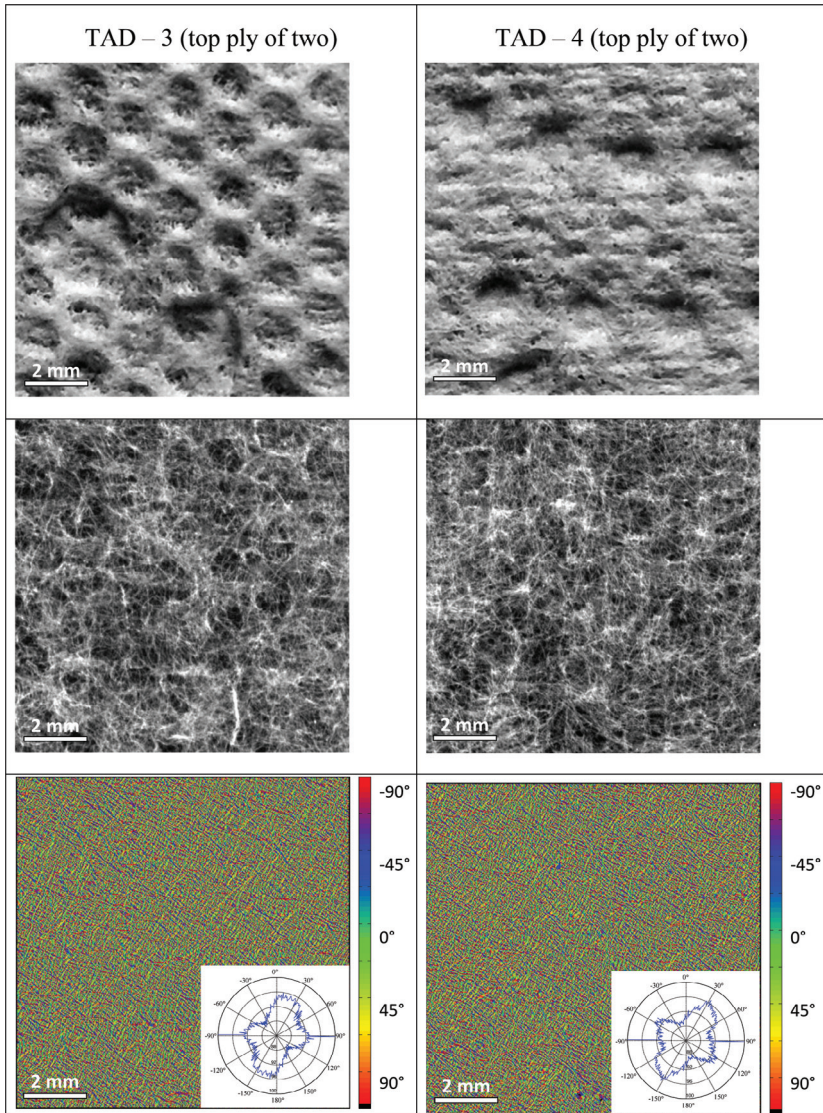


**Figure 9.** Two-dimensional orientation results for TAD – 3 (left) and TAD – 4 (right) paper towel samples. Top frame shows a photograph of the sample under  $30^\circ$  grazing angle light. The center image shows the soft X-radiographic images with side length of 10.6 mm. The lower frame shows the 2D orientation maps corresponding to the radiographic images above. An inset in the lower frame shows the polar orientation distributions for the data used to form the 2D orientation maps.

and only small differences are seen in the orientation distributions, cf. Figure 8. The primary and secondary lobes, as seen in the polar plots are not perpendicular as the larger lobe is about  $+25^\circ$  from the MD axis. This is likely the result of the effect of the pattern of the TAD features, cf. Figure 7 top. The results for TAD-4, produced by a different manufacturer show an interesting relationship between the patterns observed in the radiograph, and the measured material orientations. A regular pattern aligned in the MD with spacing of around 1 mm may be observed. This pattern does not appear to translate directly to the local material orientation as apparent in both the polar and Cartesian orientation distributions. In the polar plot, the primary peak appears to be from  $30^\circ$  to  $40^\circ$  from MD. As with TAD-3, the angle formed between the primary and secondary peaks not perpendicular, around  $80^\circ$ . From the Cartesian orientation distributions (Figure 8), the peak to base height for TAD-4 appears slightly larger as compared to TAD-1, -2 and -3.

The results for the next two samples, shown in Figure 10, are considerably different from the TAD samples seen to this point. The first, A-1, is an ATMOS (Advanced Tissue Molding System) product formed from recycled pulp as evident by the contaminant particles seen in the radiograph. One can clearly see the formed features as around 1.5 mm long ovals, and the dominant MD orientation of the fibers. In the orientation map, both the structural features and the MD oriented fibers (green) may be clearly seen. Both polar and Cartesian orientation distributions (see Figure 10 (inset) and Figure 8) quantify the pronounced MD orientation as compared to the results from TAD-1 to TAD-4 samples. TAD-5 is a single-ply product and has structural and performance properties quite different from the five preceding samples. The sample has a corrugated or creped pattern across the CD, and densified bars oriented towards the MD. While fibers must orient in MD during the initial stages of the forming process, post forming processes, such as creping appear to have realigned fibers in the cross machine direction. In fact, fiber segment orientation spans a broad range of angles from  $+20^\circ$  to  $+100^\circ$ , as seen in the polar orientation distribution in the bottom frame of Figure 10, and in the Cartesian plot in Figure 8. Close inspection of the radiograph reveals the cross machine alignment of material at a fine scale, and the sweeping arc formed between the vertical bars.

Two products formed by conventional wet pressing are shown in Figure 11. Both products appear to use recycled pulp in the furnish, although the structures appear quite different in the radiographs. Both samples have a regular fabric patterning, although it appears more intense in CWP 2. The fabric pattern is not evident in the orientation maps that appear quite similar to each other. The orientation distributions provide a clear contrast between the two samples in response to the more intense fabric patterning seen in CW-2. That sample shows much greater segment orientation toward the MD  $+10^\circ$ , as compared to the CW-1 sample. Close examination of the orientation maps also reveals subtle differences

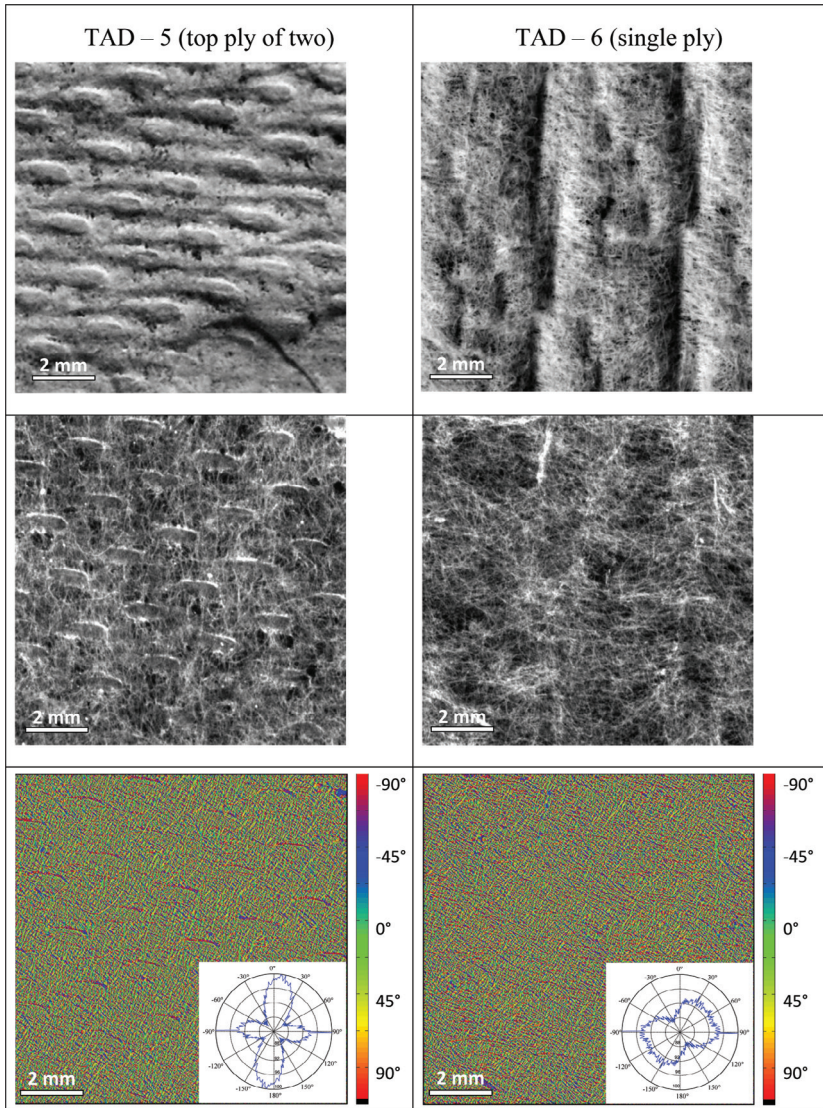


**Figure 10.** Two-dimensional orientation results for ATM – 1 (left) and TAD – 5 (right) and paper towel samples. Top frame shows a photograph of the sample under 30° grazing angle light. The center image shows the soft X-radiographic images with side length of 10.6 mm. The lower frame shows the 2D orientation maps corresponding to the radiographic images above. An inset in the lower frame shows the polar orientation distributions for the data used to form the 2D orientation maps.

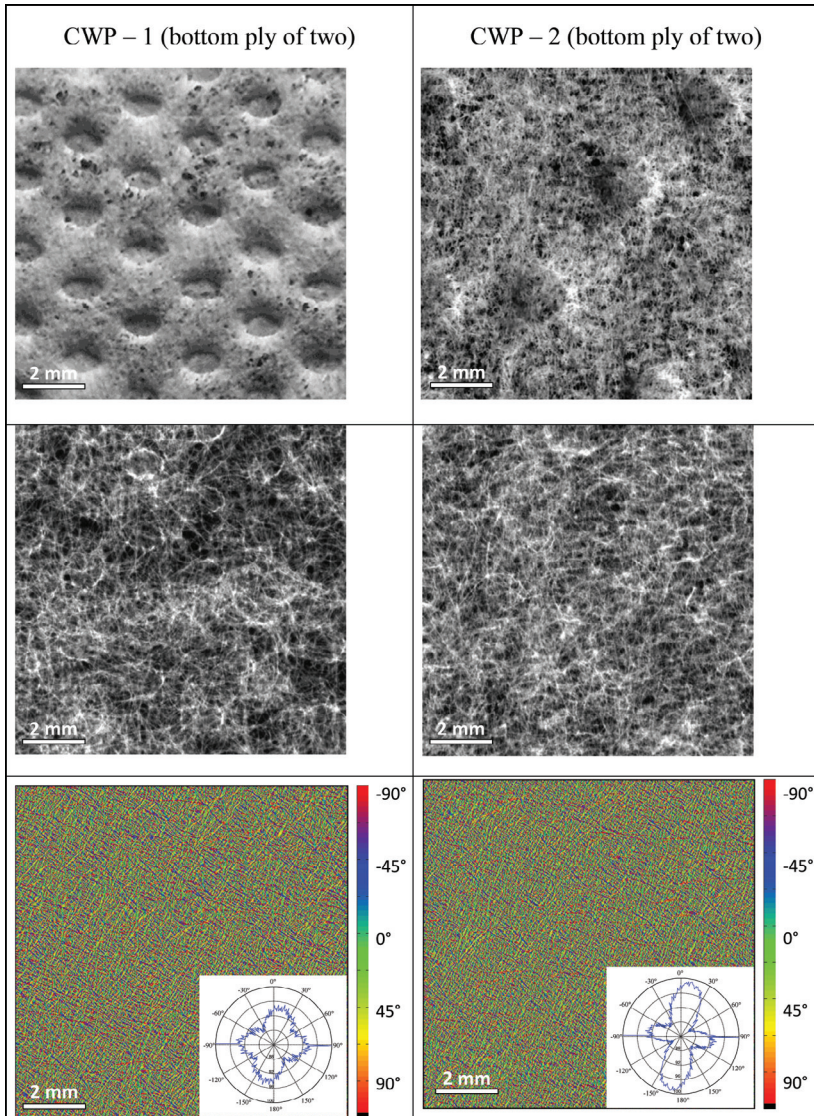


**Figure 11.** Two-dimensional orientation results for CWP-1 (left) and CWP-2 (right) paper towel samples. Top frame shows a photograph of the sample under 30° grazing angle light. The center image shows the soft X-radiographic images with side length of 10.6 mm. The lower frame shows the 2D orientation maps corresponding to the radiographic images above. An inset in the lower frame shows the polar orientation distributions for the data used to form the 2D orientation maps].

in the regional orientation, for areas of about 2–4 mm that appears to be a function of grammage. This is expected, since segment alignment will have greater variance for lower grammage regions, than those regions where higher grammage nullifies the orientation intensity. This aspect can be studied by filtering the orientation map based on the aspect ratio of the inertial ellipse. This approach was tested for the 3D orientation analysis discussed below.

To summarize, the 2D orientation analysis based on high resolution X-radiographic imaging provided a method for distinguishing and quantifying the differences between different paper towel samples. Two aspects were not examined in this study, but appear to provide a valuable application of the method. The first is to determine how fiber segment orientation depends on individual conditioning process, isolated from the influence of other processes. In this study, the materials were final products resulting from the summed response of multiple processes. Thus, it would be exceedingly difficult to identify specific origins of orientation response. Secondly, partitioning of the analysis by selecting regions associated with features, or by filtering based on grammage or aspect ratio of the inertia ellipse, may reveal subtleties unique to processes and to end use mechanical properties.

### **3D Orientation Analysis**

#### *3D Orientation maps and histograms*

The three-dimensional orientation of fibers within low density structures is represented by the colorization of tomographic projections in 3D space, where the color indicates the orientation of the inertial ellipsoid for a given location, either rotating about the z axis within the x-y plane,  $\varphi$ , or rotating about the larger of the two secondary axes showing elevation,  $\theta$ .

Figure 12 shows the results for TAD-1 using the XRadia XR- $\mu$ CT at a voxel size of 2.5  $\mu$ m and spanning a square region of about 2.5 mm. The top two frames show the 3D map for in-plane orientation,  $\varphi$ , and the Cartesian and polar plots of the orientation. Since the specimens were mounted with arbitrary orientation in the XR- $\mu$ CT analysis, the machine direction is not known. Therefore, the origin of the polar plot is set to one axis of the x-y plane of the data set. Since the tomograph shown in Figure 12 has lower resolution, fiber segmentation and fiber edge definition is not as good as for the two other methods used in this study. However, sampled region is much larger and contains five TAD features. Fibers are clearly oriented along a +45° angle, visible in the orientation map and quantified in the orientation distributions. The orientation map and orientation distribution for elevation,  $\theta$ , are shown in the bottom frames of Figure 12. The response of fibers as they ascend and descend the TAD features may be viewed as regions of orange,

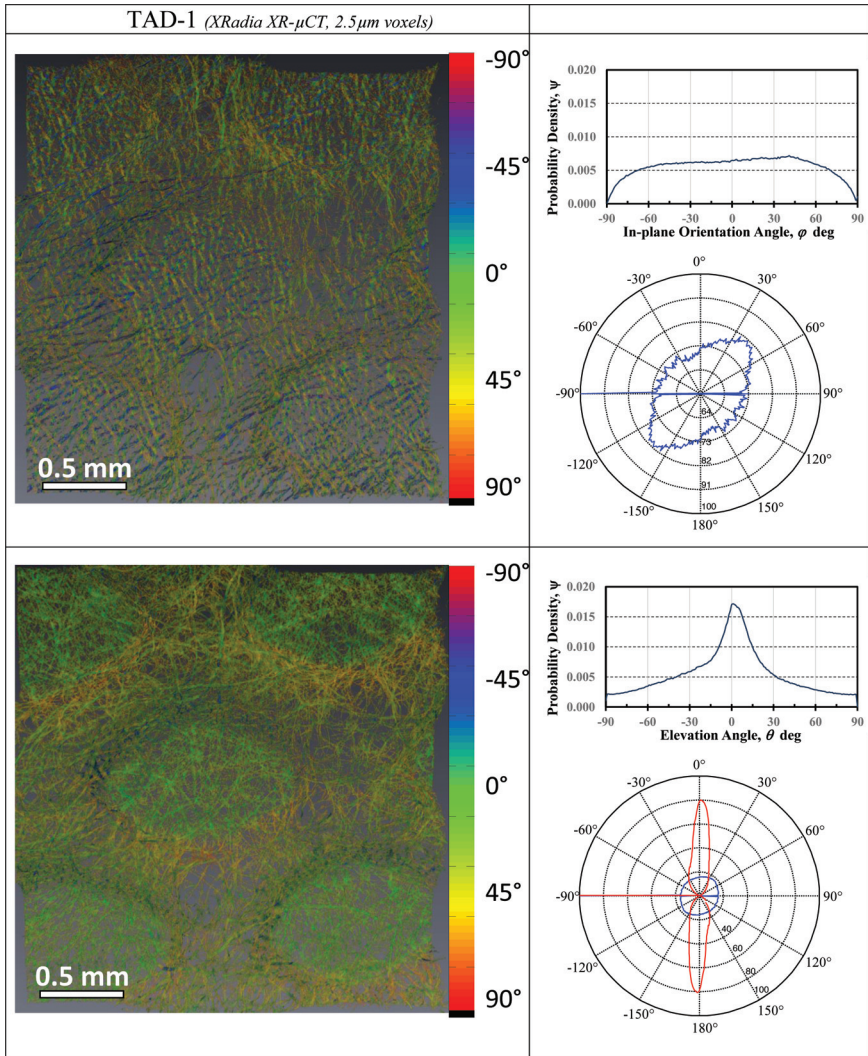
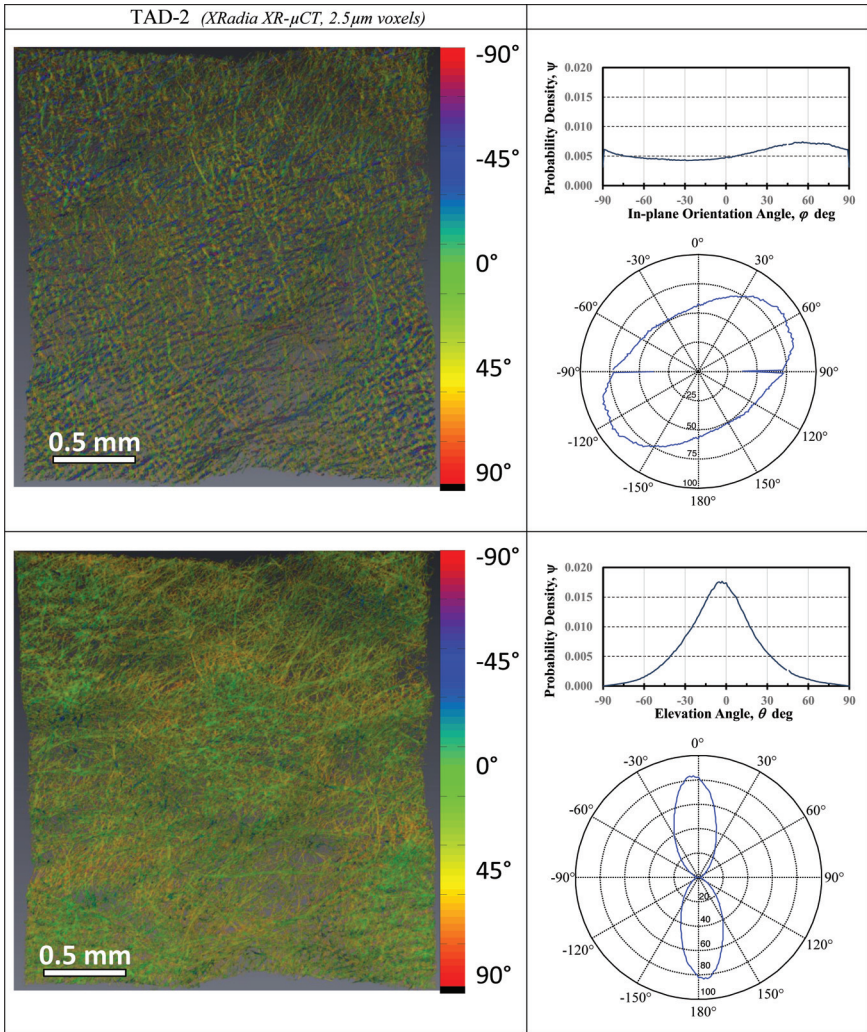


**Figure 12.** Three-dimensional orientation results for TAD – 1 paper towel sample. The top frame shows the 3D orientation map for the in-plane orientation ( $\varphi$ ) of fiber segments within the 2.5 mm square sample. In the bottom frame, the 3D orientation map for the elevation ( $\theta$ ) or inclination in the z-direction is shown for the same sample region. The Cartesian and polar orientation distributions for the in-plane orientation ( $\varphi$ ) and elevation orientation ( $\theta$ ) are shown in the left frames.

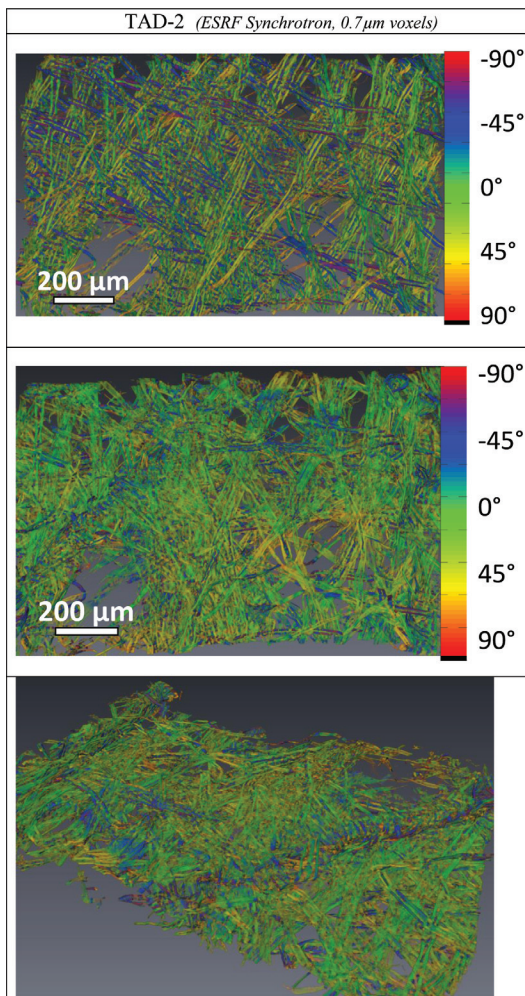
+45°, and blue, -45°, which appear at the periphery of all of the features. Regions that are parallel to the principal plane appear as green. This method therefore permits quantification of the local inclination angle that may be used to characterize local web structure. The orientation distributions for  $\theta$  shown in Figure 12 were determined from the total sample region, which is likely to be far less useful than if the orientation within sub-regions were compared. Notice that the peaks are localized near 0° which is closely aligned with the principal plane of the specimen. This indicates the dominant stratified structure of the fibers. The breadth of the distribution will be influenced by felting of the structure, as well as induced features such as embossing or TAD features.

Figure 13 shows the 3D orientation analysis for the single-ply TAD-2 sample. This data set also has a lower resolution XR- $\mu$ CT scan of about 2.5 mm square sample region was performed using the XRadia instrument. Once again, the 3D orientation map shown in the top frame, provides a clear representation of fiber segment orientation based on the inertial ellipsoid. Fibers are preferentially oriented toward an angle of +60°. It should be noted that for the current experiments, the machine direction of the samples was not indicated in the tomographic imaging. Therefore, orientation distributions do not indicate the alignment with respect to the machine direction, as was the case with the 2D analysis. This sample shows greater in-plane orientation than TAD-1 as seen in both orientation distributions. The 3D orientation map for elevation,  $\theta$ , is given in the lower frame. As compared to the TAD-1 sample, this sample shows a distinctively broader orientation distribution compared to TAD-1. Since TAD-2 is less bulky than TAD-1, the shape may be attributed more to the out-of-plane structure than felting of the fibers. Further investigation of the shape of Cartesian orientation distribution plots of elevation,  $\theta$ , may allow the separation of the effects of various bulking processes.

The 3D orientation of the TAD-2 sample was examined in more detail by using tomographic images generated from the ESRF synchrotron. The results are presented in Figure 14. The top and center frames show the sample viewed normal to the principal plane. The top frame shows the in-plane ( $\varphi$ ) orientation map. Notice that the external edges of the fibers provide an accurate representation of the angle, while the center region of the collapsed fibers is colored in contrast, suggesting perpendicular orientation. This is a manifestation of the artifact described in Materials and Methods section above, pertaining to Figure 6. This artifact seems to be sensitive to the collapsed shape of tracheids. Increased accuracy of orientation analysis would benefit from routines that address the geometry of the collapsed fibers. Nevertheless, the method does accurately reflect the orientation of the edges of the fiber segments. The center frame shows the elevation ( $\theta$ ) from a perspective normal to the principal plane. A blue arc passes from the lower left to the upper central region of the sample area. This represents a boundary in the sample where



**Figure 13.** Three-dimensional orientation results for TAD – 2 paper towel sample. The top frame shows the 3D orientation map for the in-plane orientation ( $\varphi$ ) of fiber segments within the 2.5 mm square sample. In the bottom frame, the 3D orientation map for the elevation ( $\theta$ ) or inclination in the z-direction is shown for the same sample region. The Cartesian and polar orientation distributions for the in-plane orientation ( $\varphi$ ) and elevation orientation ( $\theta$ ) are shown in the left frames.



**Figure 14.** Three-dimensional orientation results for TAD – 2 paper towel sample. The top frame shows the 3D orientation map for the in-plane orientation ( $\varphi$ ) of fiber segments within the 1.4 mm square sample. In the center frame, the 3D orientation map for the elevation ( $\theta$ ) or inclination in the z-direction is shown for the same sample region. The bottom frame show a perspective view of the 3D orientation map for the elevation ( $\theta$ ).

a TAD feature has been compressed with normal force and the fibers have buckled. The change in  $\theta$ -orientation of fiber segments within the buckled region is represented by changes in the color from the neutral green values. The bottom frame of Figure 14 provides a perspective view to show the buckled region with more clarity, passing from red-orange to blue violet as fibers kink and fold in a Z shape.

The ability to resolve creping and corrugated structures is more clearly demonstrated for the CWP-1 sample examined using tomographic images generated from the ESRF synchrotron. As shown in Figure 15. The center frame shows the view that is perpendicular to the principal plane. The alternating horizontal stripes indicate a wider region undergoing shallow incline (yellow) followed by an abrupt decline (blue-violet) in the z-direction. The perspective view provided in the bottom frame shows the spatial changes in the fibrous structure that result in the assignment of  $\theta$  values at each location. This method does not focus on the mean orientation of the entire fiber, but through the use of local orientation determination, allows the changes in orientation that fibers undergo as they pass between structural features. The figure shown in the top frame of Figure 15 shows the in-plane orientation of fiber segments. Once again, the bounding edges of the fibers accurately respond to orientation analysis, while the regions between these edges appear to provide contrary values. In an effort to address this situation, a filtering algorithm was applied, based on the geometry of the inertial ellipsoid.

#### *Filtering by Elongation of the Inertial Ellipsoid*

As demonstrated in the previous section, the precision of the 3D orientation analysis makes it susceptible to irregularities of the fibers, such as the collapsed structure with thicker bounding edges, fiber anatomy such as pits, or defects such as wrinkles, folds or cracks that can disrupt the calculation of the moment of inertia for a solid region. To address this, an approach was taken to use the geometry of the calculated inertial ellipsoid in order to segment between regions with a linear component, such as edges, or those which appear flat and planar, such as the expanse that exists in the center of collapsed fibers. To achieve this, the aspect ratios of the ellipsoid in three dimensions are considered. For edges, the resulting ellipsoid will be elongated, cf. Figure 4B, where for major axis,  $a$ , and the first minor,  $b$ , and second minor,  $c$ , orthogonal axes have the relationship:

$$a \gg b \geq c \quad (2)$$

For flat planar regions, the inertial ellipsoid will take an oblate spheroidal shape and follow the relationship:

$$a \geq b \gg c \quad (3)$$

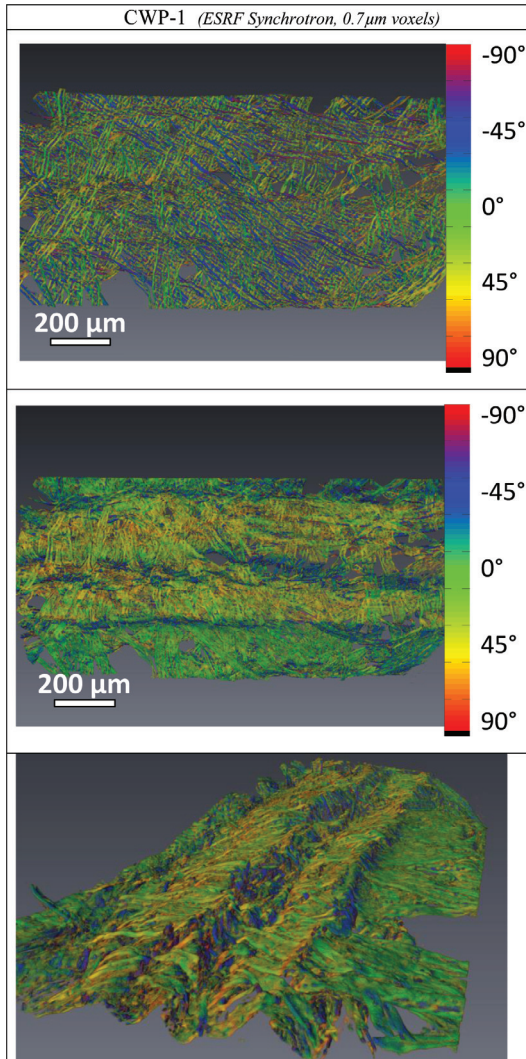


**Figure 15.** Three-dimensional orientation results for CWP-1 paper towel sample. The top frame shows the 3D orientation map for the in-plane orientation ( $\varphi$ ) of fiber segments within the 1.4 mm square sample. In the center frame, the 3D orientation map for the elevation ( $\theta$ ) or inclination in the z-direction is shown for the same sample region. The bottom frame shows a perspective view of the 3D orientation map for the elevation ( $\theta$ ).

Using these relationships, filters were applied to the 3D orientation analysis performed on the high resolution XR- $\mu$ CT data sets generated at the ESRF synchrotron. Figure 16 shows a cubic region of TAD-3 with sides of 70  $\mu\text{m}$  (100 pixels). For this example, the criterion for partitioning between edges and planar regions uses the ellipsoid dimension parameters where  $a/b > 2.5$  is considered an elongated ellipsoid and  $1 < a/b < 2.5$  approaches an oblate spheroidal shape. In Figure 16 regions that generate an elongated ellipsoid, such as the fiber edges and edges surrounding the pits are shown in green. The remaining regions, shown as gold, gave inertial ellipsoids with oblate spheroidal shape. This method was applied to sample TAD-2, with the resulting spatial representation shown in Figure 17. Once again, the fiber edges were segmented from the flat planar region of the collapsed fibers. While this method is useful at distinguishing fiber edges, it does not fully solve the proper characterization of flat planar region that should be considered to have the same orientation as adjacent edges when the mass weighted orientation is determined. This becomes more relevant if fiber orientation has dependence on fiber cross sectional geometry. Also, the inertial ellipse of those regions where fibers approach or are bonded will have a characteristic shape that might not be elongated, even if they are at an edge. This may be seen in the model fibers shown in Figure 6 for the 2D orientation analysis. Examination of the crossed regions shows a departure from the predicted fiber orientation value, as the mass of the crossing fiber contributes to the calculation. Further examination of these aspects, in future studies may shed

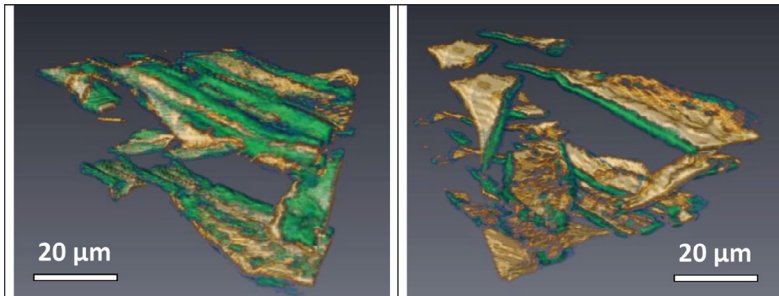


**Figure 16.** View of a  $100 \times 100 \times 100$  voxel region of TAD-1 imaged at ESRF to a resolution of  $0.7 \mu\text{m}$ . Colors represent the rotational angle for elongated ellipsoids ( $R_{1,2} > 2.5$ ) shown as green to blue, and oblate spheroids ( $1 < R_{1,2} < 2.5$ ) shown as red to yellow. Top view (on left) shows the sensitivity of the filter to the ridges that form when the lumen collapses on drying. The bottom view (on right) illustrates how voxels in flat planar regions show weak indication of mass orientation.

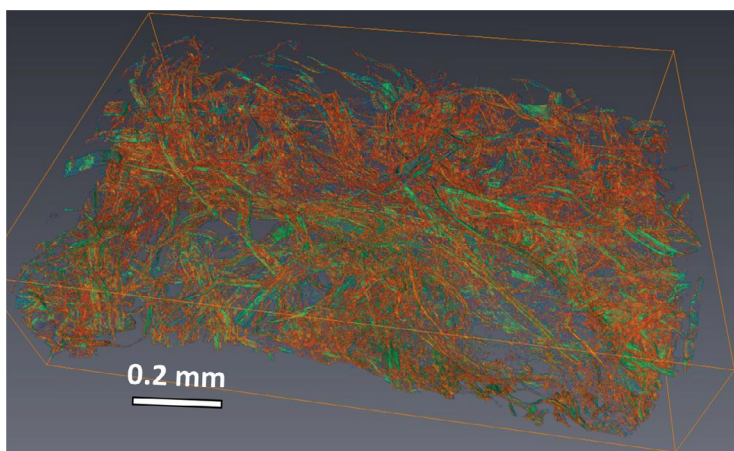


**Figure 17.** View of a  $1550 \times 1000 \times 388$  voxel<sup>3</sup> region of TAD-1 imaged at ESRF to a resolution of  $0.7 \mu\text{m}$ . Colors represent the rotational angle for elongated ellipsoids ( $R_{1,2} > 2.5$ ) shown as green to blue, and oblate spheroids ( $1 < R_{1,2} < 2.5$ ) shown as red to yellow.

insight into the bonded area, or for assessing fiber widths in the 3D analysis of low density fibrous structures.

## CONCLUSIONS

The goal of this investigation was to develop methods to determine the orientation of fiber segments contained within low density fibrous structures, specifically paper towels. Since the material had relatively large free fiber length, and a lower degree of bonding as compared to communication papers, analysis by both 2D and 3D were pursued. For the 2D analysis, a soft x-radiography method was found useful for obtaining two-dimensional images with sufficient resolution to distinguish individual fiber through the full thickness of the web. The method is capable of reliably testing  $100 \times 100 \text{ mm}^2$  regions to a pixel size of  $5.3 \mu\text{m}$ . XR- $\mu$ CT imaging of the samples, using synchrotron radiation or laboratory instruments, provided sufficient resolution of fibers for use in the 3D orientation analysis.

The 2D method for orientation analysis was based on the determination of the inertia ellipse at each position within the sampled region. Using a mass weighted calculation of the image moment, from the second order moment, for a circular region surrounding the test point, the parameters for the inertial ellipse,

including the major and minor axis lengths and the in-plane orientation angle,  $\varphi$ , at the test point. Orientation distributions for the entire region were determined as well. Orientation maps calculated from this method were produced for various paper towel samples, including products made using through air dried (TAD), conventional wet pressed (CWP) and Advanced Tissue Molding System (ATMOS) processes. The comparison revealed differences in orientation at fine scales that was dependent on the forming process, and subsequent processes that affected fiber positioning within the MD-CD plane. With the viability of the method demonstrated in this study, specific analysis of the effects of different processes on fiber orientation, and on end use properties should follow.

Using tomographic images, the investigation examined the simultaneous measurement of fiber orientation within the principal plane, and the elevation of fiber segments in the Z-direction. The method selected for this analysis consisted of determining the covariance matrix for a spherical region surrounding the test voxel, and applying principle component analysis to determine the parameters for the inertial ellipsoid defined by the mass within the region. The Euler angles were then determined, with primary focus on the in-plane orientation,  $\varphi$ , and elevation,  $\theta$ , angles to define the local orientation at each solid point within the structure. Orientation distributions for the entire region were determined, and found of minimal use due to the heterogeneity of the small regions tested by tomography. Colorized, three-dimensional projections were generated for several samples, in which regions with defined edges responded well to the analysis. However, flat planar regions, where the inertial ellipse had the shape of an oblate spheroidal shape produced results contrary to the surrounding orientation values. Further analysis was conducted to partition the orientation results using the aspect ratio of the inertial ellipsoid to distinguish between edges and planar regions.

## **ACKNOWLEDGEMENTS**

The authors wish to thank ESRF for its scientific support through the project MA127 for tomographic experiments conducted on the ID19 beamline at the European Synchrotron Radiation Facility (ESRF), Grenoble, France. We also appreciate the efforts of Dr. Greg Reese, Miami Research Computing Support group for developing the parallel code and Dr. Richard Edelmann and the Center for Advanced Microscopy & Imaging at Miami University for film development support. The technical suggestions provided by Dr. William Sampson of the University of Manchester, UK are greatly appreciated.

## APPENDIX I

### *2D Fiber Segment Orientation*

Low-order two dimensional image moments are used to determine the centroid and moment of inertia for mass represented in 2D space [37], as appropriate for grammage maps derived from X-radiographic images of tissues and towels. For a region of defined dimensions  $x$  and  $y$ , and the in-plane grammage distribution denoted by  $f(x,y)$ , all integrals are over this finite region.

The zero-order moment represents the total image mass,

$$\mu_{00} = \iint f(x, y) dx dy \quad (4)$$

the first-order moments give the position of the centroid of mass,

$$\mu_{10} = \iint x f(x, y) dx dy \quad (5)$$

$$\mu_{01} = \iint y f(x, y) dx dy \quad (6)$$

and the second order moments characterize the size and orientation of the mass,

$$\mu_{20} = \iint y f(x, y) x^2 dx dy \quad (7)$$

$$\mu_{11} = \iint y f(x, y) xy dx dy \quad (8)$$

$$\mu_{02} = \iint y f(x, y) y^2 dx dy \quad (9)$$

For the ellipse image shown in Figure 3, the semi-major,  $a$ , and semi-minor,  $b$ , axes may be derived from the equations:

$$a = \left( \frac{\mu_{20} + \mu_{02} + \left[ (\mu_{20} - \mu_{02})^2 + 4\mu_{11}^2 \right]^{1/2}}{\mu_{00}/2} \right)^{1/2} \quad (10)$$

$$b = \left( \frac{\mu_{20} + \mu_{02} - \left[ (\mu_{20} - \mu_{02})^2 + 4\mu_{11}^2 \right]^{1/2}}{\mu_{00}/2} \right)^{1/2} \quad (11)$$

The tilt angle of the ellipse is

$$\phi = (1/2) \tan^{-1} \left( \frac{2\mu_{11}}{\mu_{20} - \mu_{02}} \right) \quad (12)$$

## REFERENCES

1. T. Wahlstrom. Prediction of Fibre Orientation and Stiffness Distributions in Paper – an Engineering Approach. *Advances in Pulp and Paper Research, Oxford 2009, Vols 1–3:1039–1078*, 2009.
2. G. Lindblad. Using Ultrasonic to Predict Compression Strength. *Paper Asia* (8): 30–33, 1996.
3. A. Erkkila, P. Pakarinen and M. Odell. Sheet-Forming Studies Using Layered-Orientation Analysis. *Pulp & Paper Canada* 99(1):81–85, 1998.
4. M. Avikainen, J. Hamalainen and P. Tarvainen. Hocs Fibre: CFD-Based Software for Fibre Orientation Profile Optimization for Conventional and Dilution Headboxes. *Nord Pulp Pap Res J* 25(4):456–462, 2010.
5. H.J. Schultz and M. Kaltenecker. The First Dilution Headbox of the World – the Btf-System for Approach System, Sheet Formation and Wire Part – Industrial Experience with over 82 Plants. *Wochenblatt Fur Papierfabrikation* 126(11–12):524–527, 1998.
6. H. Altendorf. 3d Morphological Analysis and Modeling of Random Fiber Networks, Ph.D. Thesis, Centre for Morphology and Mathematics, Paris Institute of Technology and Technical University of Kaiserslautern, Fontainebleau, France, 2011.
7. H. Altendorf, E. Decenciére, D. Jeulin, P.D. Peixoto, A. Deniset-Besseau, E. Angelini, G. Mosser and M.C. Schanne-Klein. Imaging and 3d Morphological Analysis of Collagen Fibrils. *J. Microsc.* 247(2):161–175, 2012.
8. T.M. Cresson, H. Tomimasu and P. Luner. Characterization of Paper Formation .1. Sensing Paper Formation. *Tappi Journal* 73(7):153–159, 1990.
9. W.K. Ng and C.T.J. Dodson. Rapid Formation Performance Test. 1995 International Paper Physics Conference (CPPA and TAPPI) (September 11, 1995; CPPA Technical Section) pp. 49–53, 1995.
10. D.S. Keller and J.J. Pawlak. Beta-Radiographic Imaging of Paper Formation Using Storage Phosphor Screens. *Journal of Pulp and Paper Science* 27(4):117–123, 2001.
11. J.J. Pawlak and D.S. Keller. Analytical Technique for the Comparison of Paper Formation Imaging Methods. *Journal of Pulp and Paper Science* 27(5):171–176, 2001.
12. J.D. Pelgrams. A Study of the Structure of Paper by Means of “Soft” X-Rays. *Paper Trade Journal* (1):25–32, 1952.
13. H. Tomimasu, D. Kim, M. Suk and P. Luner. Comparison of Four Paper Imaging Techniques: .Beta.-Radiography, Electrography, Light Transmission, and Soft X-Radiography. *Tappi Journal* 74(7):165–176, 1991.
14. T.E. Farrington. Soft X-Ray Imaging Can Be Used to Assess Sheet Formation and Quality. *Tappi Journal* 71(5):140–144, 1988.

15. T. Yuhara, M. Hasuike and K. Murakami. Application of Image Processing Technique for Analysis on Sheet Structure of Paper. (3). Determination of the Fiber Orientation Distribution of Paper. *Japan Tappi* 41(6):523–529, 1987.
16. T. Yuhara, M. Hasuike and K. Murakami. Application of Image Processing Technique for Analysis of Sheet Structure of Paper. (2). Evaluation of the Formation of Paper. *Japan Tappi* 40(10):949–958, 1986.
17. T. Yuhara, M. Hasuike and K. Murakami. Fiber-Orientation Measurement with the Two-Dimensional Power Spectrum of a High-Resolution Soft X-Ray Image. *Journal of Pulp and Paper Science* 17(4):J110-J114, 1991.
18. C. Feng. Soft X-Ray Measurement of Low Density Materials and Compressive Response Characterization, M.S. Thesis, Chemical and paper Engineering, Miami University, Oxford, Ohio, 2012.
19. D.S. Keller, S.R. Du Roscoat and Y. Huang. Mapping the Z-Direction of Mass of Paper Towel Grades Using X-Ray Microtomography. In *2010 Progress in Paper Physics Seminar*, (ed. N. Gurnagul), FP Innovations, Montreal, 2010.
20. S.R. Du Roscoat, J.F. Bloch and X. Thibault. Synchrotron Radiation Microtomography Applied to Investigation of Paper. *Journal of Physics D-Applied Physics* 38(10A):A78-A84, 2005.
21. M. Axelsson. 3d Tracking of Cellulose Fibres in Volume Images. In 2007 IEEE International Conference on Image Processing, Vols 1–7,, pp. 2005–2008, Ieee, New York, 2007.
22. M. Wiltsche, M. Donoser and W. Bauer. Tracking of Fibers in 3d Paper Structures Obtained by an Automated Microtomy Method. In *Progress in Paper Physics*, ed, (ed. Oxford, OH, 2006).
23. M. Wiltsche, M. Donoser, J. Kritzinger and W. Bauer. Automated Serial Sectioning Applied to 3d Paper Structure Analysis. *J. Microsc.* 242(2):197–205, 2011.
24. M. Aronsson. On 3d Fibre Measurements of Digitized Paper: From Microscopy to Fibre Network, Centre for Image Analysis, Swedish University of Agricultural Sciences, Uppsala, Sweden, 2002.
25. M. Axelsson. Estimating 3d Fibre Orientation in Volume Images. In *19th International Conference on Pattern Recognition, ICPR 2008.*, pp. 1–4, 2008.
26. J.C. Tan, J.A. Elliott and T.W. Clyne. Analysis of Tomography Images of Bonded Fibre Networks to Measure Distributions of Fibre Segment Length and Fibre Orientation. *Advanced Engineering Materials* 8(6):495–500, 2006.
27. H. Altendorf and D. Jeulin. 3d Directional Mathematical Morphology for Analysis of Fiber Orientations. *Ecs10: The 10th European Congress of Stereology and Image Analysis*:113–118, 2009.
28. Tappi Standard Test Methods T410 Om-02, Grammage of Paper and Paperboard (Weight Per Unit Area). TAPPI PRESS, Atlanta, 2003.
29. Tappi Standard Test Methods T411 Om-02, “Thickness (Caliper) of Paper, Paperboard, and Combined Board. TAPPI PRESS, Atlanta, 2003.
30. Y.J. Sung, C.H. Ham, O. Kwon, H.L. Lee and D.S. Keller. Applications of Thickness and Apparent Density Mapping by Laser Profilometry. In *Advances in Paper Science and Technology: Trans. 13th Fundamental Research Symposium* Cambridge (ed.

- S.J. Panson), pp. 961–1007, Cambridge, UK. The Pulp and Paper Fundamental Research Society, 2005.
31. G. Behiels, F. Maes, D. Vandermeulen and P. Suetens. Retrospective Correction of the Heel Effect in Hand Radiographs. *Med Image Anal* 6(3):183–190, 2002.
  32. S.L. Fritz and W.H. Livingston. A Comparison of Computed and Measured Heel Effect for Various Target Angles. *Med Phys* 9(2):216–219, 1982.
  33. M. Reiss. The Cos<sup>4</sup> Law of Illumination. *Journal of the Optical Society of America* 35(4):283–288, 1945.
  34. D. Legland. Matgeom Geometric Computing Toolbox, <http://matgeom.sourceforge.net>, 2012.
  35. R. Holmstad. Methods of Paper Structure Characterization by Means of Image Analysis, Ph.D. Thesis, Norwegian University of Science and Technology, Trondheim, Norway, 2004.
  36. National Institute of Health (NIH). Imagej Image Processing and Analysis in Java. <http://rsb.info.nih.gov/ij/>, 2013.
  37. M.R. Teague. Image-Analysis Via the General-Theory of Moments. *Journal of the Optical Society of America* 70(8):920–930, 1980.

## Transcription of Discussion

# LOCAL STRUCTURAL ORIENTATION OF TOWEL AND TISSUE GRADES IN TWO AND THREE DIMENSIONS

*D. S. Keller,<sup>1</sup> C. Feng,<sup>1</sup> J.- F. Bloch<sup>2</sup> and  
S. Roland du Roscoat<sup>3</sup>*

<sup>1</sup> Miami University, Department of Chemical, Paper, and  
Biomedical Engineering, Oxford, OH, USA

<sup>2</sup> Grenoble Institute of Technology, 38402 Saint Martin d'Hères, Cedex, France

<sup>3</sup> Université Joseph Fourier, Domaine Universitaire, 38041 Grenoble,  
Cedex, France

*Steve I'Anson*      FRC Chairman (from the chair)

Steve, when you talk about spatial partitioning of the images, is it the intention to use something like the Fourier transform to filter out a specific pattern using one type of image and use that as a template to look for correlations in the others? I do not know if you could do that in three dimensions but you certainly can do it in two.

*Steve Keller*

I would probably use either two or three dimension image fusion (or both). The simplest example is to take the out-of-plane deformation map and from the upper limits identify regions that are high points on the sample and then selectively look at the orientation data for those regions. Partitioning by grammage values would be an alternative method to consider. For this, one would take the three dimensional grammage projection, like the ones I showed, and use that to partition into different regions. For example, the top or base of the domes or creping regions where mass values are high and can be separated out to observe the local orientation.

## *Discussion*

*Steve I'Anson*

My idea is, for example, that, if you thought you might have a wire mark as well as the TAD mark, you could actually just filter for the wire mark and look at whether it's causing any differences in orientation.

*Steve Keller*

It would also be possible to look at dimensional change (shrinkage or stretch) that was occurring within the structure during drying, using the wire marks that you could filter out from this. That's a very good idea, best done in the, 2D images I would say.

*Ulrich Hirn*      Graz University of Technology.

You have used a rather elaborate method to calculate the local orientation. As I understand it, the standard method is the one proposed by Erkkilä et al.<sup>1</sup> at the end of 90's. You just compute the local gradients of the density and you can derive anisotropy and orientation straightforwardly from that. I just want to ask what is the advantage of your method and why did you choose to use another method when this method is well established?

*Steve Keller*

So, does that method look at density gradients in three dimensions within the structure?

*Ulrich Hirn*

They did it in 2D but it would be straightforward to generalise it to 3D, just by adding the z-directional gradient.

*Steve Keller*

Well, it sounds like that would be a good thing to look at. I will look into a comparison between the two approaches. Thank you for the suggestion.

<sup>1</sup>A.-L. Erkkilä, P. Pakarinen and M. Odell, "Sheet-Forming Studies Using Layered-Orientation Analysis", Pulp & Paper Canada 99(1):81-85, 1998.

*Bill Sampson*      University of Manchester

Steve, there are two parts to my question. Firstly, you talked about low density webs, but they had low grammage also: have you looked at papers which have low density but high grammage? Secondly, your method may be quite a nice way to finally build upon what Prof. Dodson did in 1965<sup>2</sup>, looking at filtering and layering in forming processes, and to quantify how much three-dimensionality there is in non-embossed papers.

*Steve Keller*

We have not looked at the low-density, high-grammage papers, although it would be interesting. The thing that would limit the effectiveness of tomographic imaging in this case is the span of the region which you can study. The high thickness associated with high-grammage/low-density papers, along with the dimensions of the in-plane region, would create a very large data set. For now, I have had to confine the data set to sizes that can be managed in our computers. I did not select these low-grammage papers because I was looking for small data sets, but five days of calculation are required with low-grammage data and, potentially, one is looking at 50 days for a high-grammage data set. What we are doing is to try to perfect the analytical approach on samples where we can visualise individual fibres and we will then apply the knowledge we have gained from low-grammage webs to higher grammage papers.

However, I think the stratification of different structures within webs is going to be something where our approach will have plenty of application. The criticisms that have been brought up in the past arise from the small size of the regions that have been examined with micro x-ray CT, typically limited to 2 mm or 5 mm. That is, where the validity of such data for representing real world systems comes into question. Where we use much larger regions we will be able to correlate results for the two-dimensional maps, which can easily be created at a larger size, with the three-dimensional projections, so we can obtain both scale and precision.

*Daniel Söderberg*      KTH and Innventia

Steve, we did some work in two dimensions with steerable filters as a tool for analysing fibre orientation which turned out to be very efficient. I imagine that there are ways of doing that in 3D also. Have you looked at that?

<sup>2</sup>B. Radvan, C.T.J. Dodson and C.G. Skold. "Detection and cause of the layered structure of paper". In Consolidation of the Paper Web, *Trans. IIIrd Fund. Res. Symp. Cambridge, 1965*, (F. Bolam, ed.), pp 189–214, FRC, Manchester, 2003. ISBN: 0 9541126 3 6.

*Discussion*

*Steve Keller*

No, I have not examined that method in either two or three dimensions. The purpose of our work was to investigate a new technique for finding local orientation. This is a good suggestion for us to compare with our results in the near future.